Programmable higher-order Euler buckling modes in hierarchical beams

M.G. G Tarantino, K. Danas

Programmable higher-order Euler buckling modes in hierarchical beams

M. G. Tarantino[a], K. Danas,[a,*]

[a] *LMS, C.N.R.S., École Polytechnique, 91128 Palaiseau, France*

Abstract

We present a numerical-aided experimental study on the buckling of hierarchical beams comprising multiple self-similar modules. Each module consists of multiple elemental beams and is arranged in series to form the hierarchical beam. We show, through a combination of experiments and computations, that these beams exhibit stable and realizable higher-order buckling modes. By contrast to the canonical Euler buckling problem, such modes emerge naturally in the proposed self-similar beams since they correspond to almost identical critical loads. By harnessing the imperfection sensitivity of the hierarchical structures, we 3D-print weakly imperfect polymer samples with a small geometric imperfection corresponding to the desired eigenmode. We subsequently carry out uniaxial compression experiments and show in practice that higher-order patterns can be triggered selectively upon buckling. Moreover, these patterns are preserved in the post-bifurcation regime in many cases and are reversible upon load release. The ability to trigger higher-order buckling modes is found to depend on two main geometrical parameters which lead to scale coupling. Those are the slenderness of the macroscopic hierarchical beam and the slenderness of the lower-scale elemental beam. With increasing slenderness of the hierarchical beam, we observe a significant softening in the overall stress-strain response and patterns exhibiting curvature localization in the post-bifurcation regime. The numerical finite-strain simulations carried out in the present study are found to be in very good agreement with the experiments and are used to quantify further the observed curvature localization in the hierarchical beams. The present study and the obtained results are geometric in nature and thus can be extended to different scales and hierarchies *ad infinitum*.

Key words: Mechanical instability, Beam buckling, Imperfection Sensitivity, Post-bifurcation, Buckling-induced patterns, 3D-printing, Curvature localization

1. Introduction

Harnessing geometrical instabilities (such as buckling) to achieve programmable patterns and curvature is a challenge of current soft matter physics and mechanics. Soft materials represent an ideal platform for designing systems that may reversibly change curvature or shape when instabilities and buckling set in (Kochmann and Bertoldi, 2017). Instabilities in soft matters yield a number of geometrical features (Li et al., 2012). The latter can be activated spontaneously in stimulus-sensitive polymers, e.g. swelling gels (Trujillo et al., 2008; Lee et al., 2012), electrically-switching

*Corresponding author.

Email addresses: maria-gabriella.tarantino@polytechnique.edu (M. G. Tarantino), konstantinos.danas@polytechnique.edu (K. Danas,)

liquid crystals (Camacho-Lopez et al., 2004; Danas et al., 2018), electro- (Jager et al., 2000; Wang and Zhao, 2013) and magneto-active elastomers (Danas and Triantafyllidis, 2014; Gerbal et al., 2015; Huang et al., 2016; Psarra et al., 2017). Alternatively, they can be selectively controlled through a rational geometry design, e.g. in film/substrate blocks (Audoly and Boudaoud, 2008; Chen and Hutchinson, 2004; Huang and Suo, 2002; Cai et al., 2011; Xu et al., 2014; Huang, 2005) and in layered structures (Stoop et al., 2015; Liu et al., 2012). Over the past decade, periodic porous elastomers have particularly attracted great attention. When deformed under compression, these materials may undergo complex, yet reversible, pattern transformations. Recent examples include holey systems transforming into a periodic pattern of alternating mutually orthogonal ellipses (Mullin et al., 2007; Javid et al., 2016), geometrically frustrated triangular cellular structures that lead to either chiral and symmetric patterns (Kang et al., 2014) as well as hexagonal honeycombs resulting, upon bifurcation, into three different deformed configurations (Papka and Kyriakides, 1999a,b; Combescure et al., 2016). More interestingly, when elastic instabilities are exploited along with structural hierarchy, as shown for hierarchical hexagonal honeycombs (Ajdari et al., 2012; Haghpanah et al., 2014; Combescure and Elliott, 2017), non-conventional mechanical properties are obtained (Sun and Pugno, 2013; Mousanezhad et al., 2015).

Structural hierarchy has been widely introduced into synthetic systems with the goal of re-examining the mechanical property space of low-density cellular solids. To date, a large body of theoretical and experimental work has been dedicated to exploring two-dimensional (2D) honeycombs with hexagonal (Ajdari et al., 2012; Sun et al., 2014; Oftadeh et al., 2014; Ryvkin and Shraga, 2018), square (Zhu et al., 2012; Mousanezhad et al., 2016) and triangular cells (Taylor et al., 2011). Whether these architectures are employed in sandwich- (Kooistra et al., 2007; Fan et al., 2008; Russell et al., 2009) or in lattice-systems, they show superior elastic and fracture properties when compared to their non-hierarchical counterparts. Moreover, the versatility of current manufacturing techniques have greatly extended the breadth of novel materials that derive properties from geometry. Notable, yet very recent, examples include three-dimensional (3D) hierarchical lattices (Meza et al., 2015; Zheng et al., 2016) built using self-similar octet-truss unit cells (Deshpande et al., 2001), as well as 3D-printed random porous polymers with three or more different families of void sizes (Zerhouni et al., 2019). Such systems efficiently incorporate multiple orders of hierarchy and contain structural features that span several order of magnitude in length scale. By virtue of their tunable response, such examples encourage the pursuit of novel hierarchical metamaterials that combine architecture with desired properties and functions.

Consider now, the simplest plane geometry one can think of, namely a slender beam. When the latter is made out of an elastic material and is subjected lenght-wise to a compressive force P, it buckles upon reaching a critical load value. The Euler buckling problem is a canonical subject of mechanics for which multiple sinusoidal-like modes (denoted with $n \in \mathbb{N}$) with different wavelengths are obtained theoretically (see for instance Timoshenko and Gere (1936)). Yet, in practice, a homogeneous beam buckles into a half sinusoid (with a number of half-waves $n = 1$) when P equals the Euler critical load $P_E = \pi^2 EI/l^2$ (with E, I and l denote respectively the Young's modulus, the cross-sectional moment of inertia and the length of the elemental homogeneous beam). The reason is that for a homogeneous beam, higher buckling modes (i.e. $n > 1$) occur at loads n^2-times higher than P_E, i.e. $n^2\pi^2 EI/l^2$, and therefore they never emerge naturally.

The aim of this study is to exploit structural hierarchy along with mechanical instability, such as buckling, to achieve selectively Euler buckling modes with $n = 1$, 2 and 3 in soft materials. Here, we take inspiration from studies on the hierarchical octet-truss and hexagonal honeycombs

lattices (Fig. 1a and Fig. 1b respectively) and apply a similar hierarchical design principle to a slender beam geometry (Fig. 1c). We thus create 2D second-order hierarchical beams comprised of multiple self-similar modules, and employ them to revisit the canonical Euler buckling problem. Our (2^{nd}-order) beams have a simple self-similar architecture, where an elemental module (1^{st}-order), consisting of a regular array of homogeneous (0^{th}-order) elemental beams in parallel, is repeated N_m-times along the direction of its longest axis. The process of making the hierarchical beam is illustrated in (Fig.1c-top) for a system containing four elemental modules. Moreover, it is highly versatile and engenders a virtually unbounded potential design space, see Fig. 1c (center and bottom respectively).

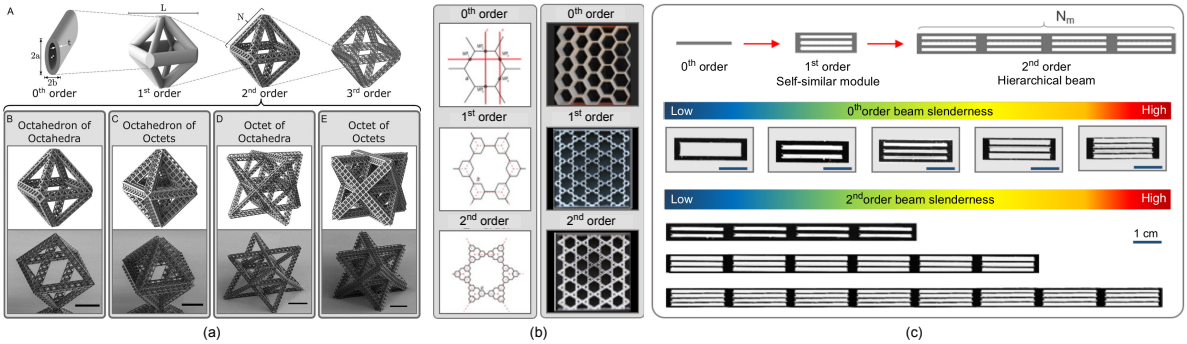

Figure 1: Hierarchical design of cellular solids. (a) Computer-aided design and scanning electron microscopy images of various third-order 3D nanolattices comprised of hierarchical octet-truss unit cells. After Meza et al. (2015). (b) Schematic and optical images of the second-order hexagonal honeycombs. After Ajdari et al. (2012). (c) 2D hierarchical beams of this work. The process of making the second-order hierarchical beam is shown at the top. A 0^{th}-order repeating element, i.e. a rectangular beam, is staggered into a 1^{st}-order elemental module. The latter is patterned along the direction of its longest-axis to create the macroscale 2^{nd}-order beam. The versatility of the design strategy enables exploring a wide range of geometrical parameters. Of interest in this study are the slenderness of the 0^{th}- and 2^{nd}-beam (center and bottom respectively).

By combining experiments, numerical simulations and high-precision polymer 3D-printing, we show that introducing hierarchy into a simple beam's architecture enables the attainment of a unique combination of functionalities. Unlike its non-hierarchical counterpart, a hierarchical beam under compression exhibits higher-order buckling modes with $n = 1$, 2 and 3 that correspond to almost identical critical loads. When such modes are properly introduced into the hierarchical beam's architecture via 3D-printing, they can then persist in a real experiment (see videos in the Electronic Supplementary Material). Moreover, the use of a rubber-like material for 3D-printing leads to a fully reversible response. To trigger selectively pattern transformation, our strategy is simple and relies on earlier seminal studies on the buckling of imperfection-sensitive structures (Hutchinson and Koiter, 1970; Tvergaard, 1973).

This paper is organized as follows. In Section 2, we carry out the bifurcation analysis of a single array of elemental beams in series. The method used is based on the beam-column solution presented in Timoshenko and Gere (1936) and relies on assuming simplified, yet rigorous, modes of buckling. In Section 3, we study the bifurcation of the full-scale hierarchical beams in Fig. 1c by means of Finite Element (FE) simulations. Specifically, we investigate systematically the effect of varying the slenderness of both the 0^{th}- and 2^{nd}-order beams. In Section 4, we investigate both experimentally and numerically the compressive deformation of the hierarchical beams in the post-bifurcation regime. The findings presented aim at elucidating how buckling instabilities at different length scales operate and interact in a self-similar hierarchical beam. Results are discussed

in Section 5 and conclusions are drawn in Section 6.

2. Analytical bifurcation analysis

In this section, we study analytically the stability of the 2D hierarchical beam in Fig. 1c subjected to uniaxial compression. Specifically, our goal is to derive a closed-form expression for the macroscopic buckling load, and in turn predict the corresponding buckling mode(s). The approach we follow is based on the classical beam-column solution which provides an expression for the end rotations of an axially loaded beam as a function of its end moments. The derivation of this formula is presented in Chapter 1 of Timoshenko and Gere (1936). To date, the beam-column method has been widely used to obtain analytically the buckling strength of various 2D cellular structures under uniaxial and biaxial loadings. Examples include honeycombs with triangular (Kang et al., 2014; Haghpanah et al., 2014), square (Bažant and Christensen, 1972; Haghpanah et al., 2014; Fan et al., 2009) and hexagonal unit cells (Haghpanah et al., 2014). In particular, Haghpanah et al. (2014) have also applied the method to hierarchical honeycombs.

We first discuss the primary features of buckling of the hierarchical beams in Fig. 1c (Section 2.1) and then use the beam-column method to solve the eigenvalue-eigenvector problem of a representative continuous beam (Section 2.3). Specialized solutions for the beam-column with a lateral end displacement are derived in Section 2.2. Note, however, that the present study relies on *a priori* defined primary modes of buckling and has therefore to be complemented with a full-scale eigenvalue analysis. This is carried out using FE simulations and is presented in Section 3. Nevertheless, the analytical findings that follow provide a simple, yet rigorous, interpretation of the bifurcation problem at hand. It should be mentioned that the following simplifications hold near the bifurcation point and cannot be extended to the case where the post-bifurcated response exhibits softening and localization. The latter is analyzed rigorously by full-field FE simulations (Section 5).

2.1. Definition of the model problem and assumptions

The hierarchical beams of this work (Fig. 1c) are 2D framed structures where every individual beam is susceptible to buckling under compressive load (see also Chapter 2 of Bazant and Cedolin (2010)). Unlike regular 2D lattices (Fan et al., 2008; Ohno et al., 2004; Haghpanah et al., 2014), these structures are not periodic. As a consequence, their buckling patterns are not *a priori* periodic either.

To analyse the primary features of buckling of the proposed structures, we consider a clamped four-module hierarchical system where elastic beams of length L, denoted henceforth as elemental beams, are rigidly connected at their nodal joints (see Fig. 2a). We anticipate here that the results presented below are independent of this choice. When subjected to a uniaxial compressive force P, the system buckles upon reaching a critical load value. Fig. 2b shows the long-wave mode of buckling for the underformed system in Fig. 2a. For every single elemental beam, the buckled shape may be different and is described by four kinematic variables, i.e. the lateral displacement δ and the rotation θ of the end nodes (see e.g. the blow-up of Fig. 2b). Due to the large number of unknown nodal rotations and displacements, solving for the stability of the system in Fig. 2a using the beam-column method does not prove amenable to an analytical treatment. Nor, it allows an intuitive understanding of the corresponding buckling patterns.

In an attempt to reduce the number of nodal kinematic variables and make the model problem tractable analytically, we make the hypotesis that, upon buckling, the rotation of the connecting

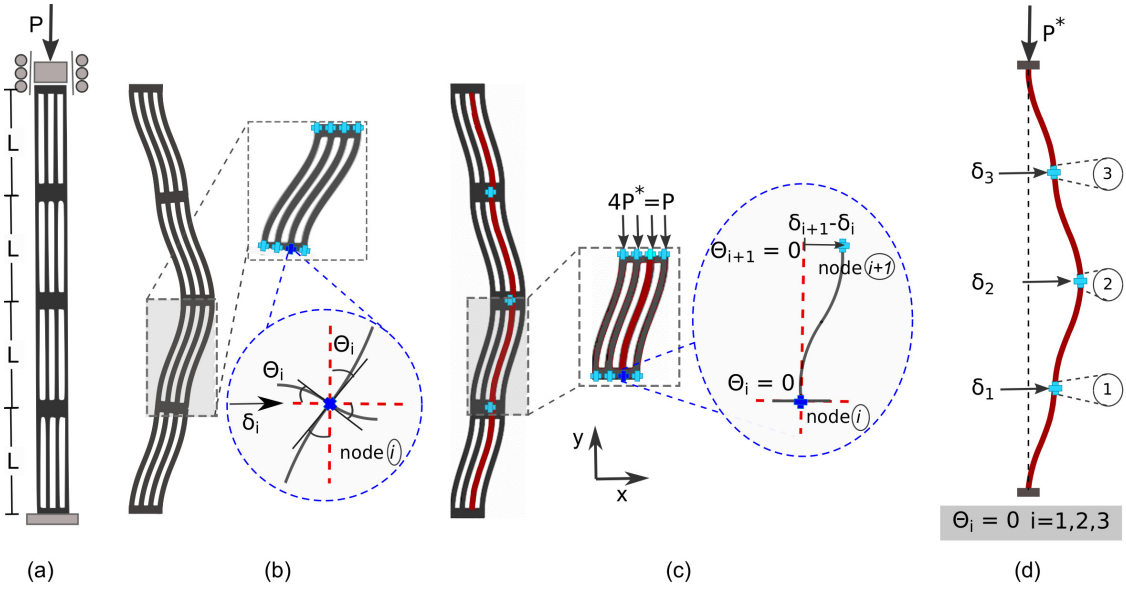

Figure 2: Approximate schemes for the buckling of the hierarchical beams. (a) Schematic of a hierarchical beam comprising $N_m = 4$ modules. Every module in turn consists of four elemental beams of length L. The structure has both ends fixed and is subjected to a macroscopic uniaxial compression. (b)-(c) Long-wave mode of buckling of the hierarchical beam in (a) involving buckling of the elemental beams. The latter have either different and identical buckled shapes, see the blow-ups in (b) and (c) respectively. Identical buckled shapes are obtained when the rotation of the connecting nodes is null. In this case, the ensemble of the elemental beams in the module can be replaced by a single elemental beam (highlighted with dark red color in every module). (d) When nodal rotation is null, the deformed configuration of the representative continuous beam is described by the lateral displacements of the connecting nodes ①, ② and ③.

nodes can be neglected. Our assumption is plausible given that the bending stiffness, of the members connecting the elemental beams in the module, is very large (see Fig. 2a). The validity of our assumption is also corroborated by the analogy with a battened column, for which the analysis of stability is presented in Chapter 2 of Timoshenko and Gere (1936). If we also make the assumption[1] that every elemental beam is subjected to the same compressive force P^* (see Fig. 2c), we can then replace the collective response of all elemental beams in the module with a single representative elemental beam. This is highlighted with dark red color in the zoom of Fig. 2c. The buckled shape of such a beam is now described by a single degree of freedom, namely the relative lateral displacement of its end nodes (see zoom of Fig. 2c). The reader is again referred to the battened column presented in Timoshenko and Gere (1936). With all above assumptions, each vertical line-beam (see e.g. the dark red beam in Fig. 2c-left) can be independently analyzed as a continuous beam comprised of four elemental elemental beams. The end nodes of each elemental beam are free to translate horizontally but are prevented from rotating, as sketched in Fig. 2d. This system now has only three degrees of freedom, namely the lateral displacements of the connecting nodes. The analysis is straightforward for any number of elemental beams but does not add any additional understanding and hence is not carried out here.

[1]This assumption is valid in the pre-bifurcation regime and also early after bifurcation provided that no softening is observed in the overall response of the hierarchical beam. The reason is that the applied macroscopic compressive force P is equally distributed among the four elemental beams set in parallel in the module.

2.2. Beam-column solution under lateral end displacement

We start by recalling the derivation of the beam-column solution of an axially loaded beam under a lateral end displacement. This solution provides a closed-form expression that links the end moments with the applied end lateral displacement. To this end, we consider a fixed end beam connecting the nodes ① and ②. The beam is subjected to a compressive force P^* as well as to a lateral displacement δ applied at end ②, see Fig. 3a. We denote respectively with L and EI the length and the bending stiffness of the beam. Fig. 3b shows the free body diagram of the beam in Fig. 3a. To derive the beam-column solution, we start by applying the condition of compatibility of the rotation θ at each end node i with $i = 1, 2$, such that

$$\begin{cases} \theta_{1,M_1} + \theta_{1,M_2} + \theta_{1,\delta} = 0 \\ \theta_{2,M_1} + \theta_{2,M_2} + \theta_{2,\delta} = 0, \end{cases} \tag{1}$$

where subscripts (i, δ), (i, M_1) and (i, M_2) denote the rotation at the end node i produced by the displacement δ and the end moments M_1 and M_2 respectively. Since the problem is linear elastic, we can superimpose effects to express each individual term in Eq.(1). For illustration purposes, we show in Fig. 3c and Fig. 3d respectively the end rotations produced by the applied moment M_1 and displacement δ.

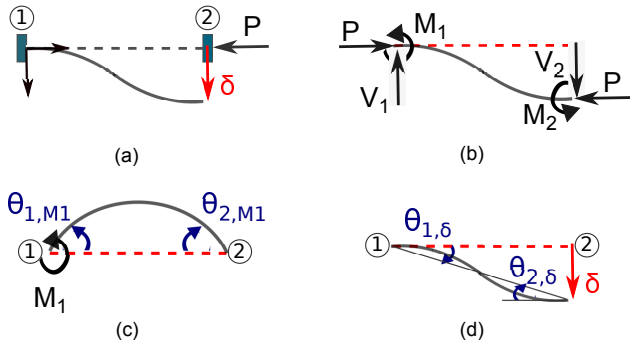

Figure 3: Schematic of (a) a fixed ends beam-column with a lateral end displacement and (b) its free-body diagram. The undeformed configuration of the beam is depicted by the dashed line connecting the end nodes ① and ②. (c)-(d) Linear superposition of the effects showing the deformed configurations of the beam produced respectively by the end-moment M_1 and the lateral displacement δ.

An expression for the end rotations produced by M_1 and M_2 is presented in Chapter 1 of Timoshenko and Gere (1936) and is also given in a number of recent papers, e.g. Fan et al. (2009); Haghpanah et al. (2014); Kang et al. (2014). Using a positive sign for rotations that bend the beam axis upwards, we write

$$\begin{cases} \theta_{1,M_1} + \theta_{1,M_2} = \dfrac{L\beta}{EI} M_1 + \dfrac{L\alpha}{EI} M_2, \\ \\ \theta_{2,M_1} + \theta_{2,M_2} = -\dfrac{L\alpha}{EI} M_1 - \dfrac{L\beta}{EI} M_2, \end{cases} \tag{2}$$

with

$$\beta = \frac{1}{kL}\left(\frac{1}{kL} - \cot(kL)\right), \quad \alpha = \frac{1}{kL}\left(\frac{1}{kL} - \csc(kL)\right). \tag{3}$$

with $k^2 = P^*/EI$. We now need to provide an expression for the end rotations produced by the lateral displacement δ, as shown in Fig. 3d. Under the assumption of small deflections, the latter produces a rigid rotation of magnitude

$$\theta_{1,\delta} = -\theta_{2,\delta} = -\frac{\delta}{L}. \tag{4}$$

Substituting Eq.(4) together with Eq.(2) into Eq.(1), we obtain a system of two linear equations which links the end moments M_1 and M_2 with the applied displacement δ. Moreover, it provides the solution for a beam-column under lateral end displacement and reads

$$\begin{cases} \dfrac{L\beta}{EI}M_1 + \dfrac{L\alpha}{EI}M_2 - \dfrac{\delta}{L} = 0, \\ -\dfrac{L\alpha}{EI}M_1 - \dfrac{L\beta}{EI}M_2 + \dfrac{\delta}{L} = 0. \end{cases} \tag{5}$$

Solving Eq.(5) for M_1 and M_2 yields

$$M_1 = M_2 = \frac{6EI}{L^2}\left(\frac{1}{2g_D - g_I}\right)\delta, \tag{6}$$

where g_D and g_I are the so called stability functions and are defined as

$$\begin{aligned} g_D &= \frac{3}{kL}\left(\frac{1}{kL} - \cot(kL)\right), \\ g_I &= \frac{6}{kL}\left(\csc(kL) - \frac{1}{kL}\right). \end{aligned} \tag{7}$$

In the interest of the analysis that follows, we find an expression for the end shear forces by applying equilibrium of the moments about the end node. This is given by

$$\begin{aligned} V_2 = V_1 &= \frac{M_1 + M_2}{L} - \frac{P^*}{L}\delta = \\ &= \frac{12EI}{L^3}\left(\frac{1}{2g_D - g_I} - \frac{k^2L^2}{12}\right)\delta. \end{aligned} \tag{8}$$

This concludes the bifurcation solution of an axially loaded elemental beam under lateral end displacement.

2.3. Stability of the representative hierarchical model beam

We determine next the critical load of the representative hierarchical model beam shown in Fig. 4a, where the rotation θ of the connecting nodes is blocked. Buckling of this system is a shear-like deformation where every elemental beam undergoes a rigid body rotation upon buckling. Such a rotation is, in turn, produced by the relative displacement of the end nodes, which are free to slide. To find the critical load of the model beam, we write the equilibrium of the shear forces at nodes ①, ② and ③ in Fig. 4a. Since there are no external lateral forces applied, equilibrium requires that the total shear force at every node $i = 1, 2, 3$ is zero, i.e.,

$$\begin{cases} V_1 = V_{1,\delta_1} + V_{1,\delta_2} + V_{1,\delta_3} = 0, \\ V_2 = V_{2,\delta_1} + V_{2,\delta_2} + V_{2,\delta_3} = 0, \\ V_3 = V_{3,\delta_1} + V_{3,\delta_2} + V_{3,\delta_3} = 0, \end{cases} \tag{9}$$

where e.g. V_{1,δ_1} is used to denote the shear force at node ① produced by the unknown generalized displacement δ_1, see Fig. 2d. Using results of Eq.(8) and imposing continuity of forces and displacements from adjacent beams, Eq.(9) becomes

$$\begin{cases} V_1 = 2V^*\delta_1 - V^*\delta_2 = 0, \\ V_2 = -V^*\delta_1 + 2V^*\delta_2 - V^*\delta_3 = 0, \\ V_3 = -V^*\delta_2 + 2V^*\delta_3 = 0. \end{cases} \tag{10}$$

with

$$V^* = \frac{12EI}{L^3}\left(\frac{1}{2g_D - g_I} - \frac{k^2L^2}{12}\right). \tag{11}$$

This last result is obtained from Eq.(8) after setting $\delta = 1$. Recasting now Eq. (10) into a matrix

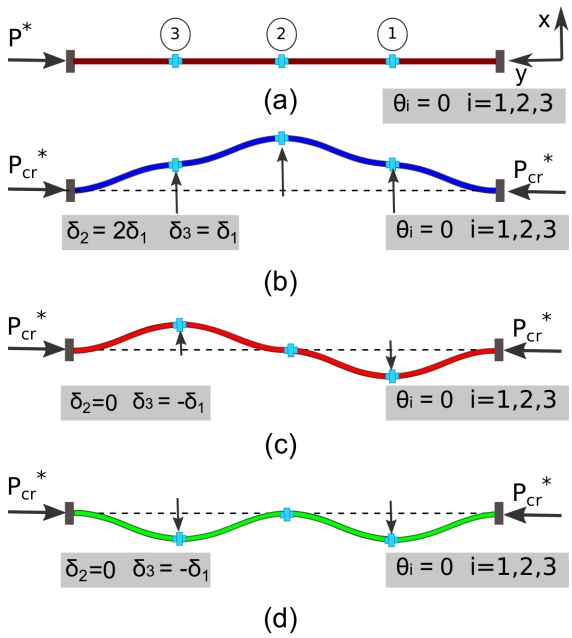

Figure 4: (a) Representative continuous beam comprised of $N_m = 4$ elemental beams with blocked end rotations. (b-c) Qualitative $N_m - 1 = 3$ buckling modes for the model hierarchical beam in (a). These modes correspond to equal critical loads.

form gives the *stability* matrix, namely

$$\begin{bmatrix} 2V^* & -V^* & 0 \\ -V^* & 2V^* & -V^* \\ 0 & -V^* & 2V^* \end{bmatrix} \begin{bmatrix} \delta_1 \\ \delta_2 \\ \delta_3 \end{bmatrix} = \begin{bmatrix} 0 \\ 0 \\ 0 \end{bmatrix}. \tag{12}$$

For non-trivial solutions of Eq.(12), one needs to set the characteristic equation of the linear system of equations for δ_i (i.e., the det of the above 3×3 matrix) equal to zero. This leads to

$$[1 + \cos(kL)]^3 = 0 \quad \text{or} \quad kL = (2q+1)\pi, \quad q \in \mathbb{N}. \tag{13}$$

The lowest critical load corresponds to $q = 0$ and is in turn given by

$$P^*_{cr} = k^2 EI = \frac{\pi^2 EI}{L^2}, \tag{14}$$

which is the well-known Euler buckling load for a fixed-fixed slope beam. The Supplemetal Material of Haghpanah et al. (2014) presents the derivation of this result using the the beam-column method. Eq.(14) also implies that irrespective of its length, the representative hierarchical beam buckles as early as $P^* = P^*_{cr}$. Our finding is in agreement with earlier studies on buckling of regular grids. Notably, Wah (1965) has shown that the buckling strength of a square grid under axial compression reduces to the buckling strength of the cell walls when these are treated as side-swaying columns with fixed slope at both ends. As observed by Haghpanah et al. (2014) for regular square grids, the result of our analysis, i.e. Eq.(14), is an upper bound estimate of the actual buckling load since it ignores rotational compliance of the connecting nodes.

Finally, substituting Eq.(14) into Eq.(12) yields an equation which is identically satisfied. Interestingly, we find that the solution of the stability equation, i.e. Eq.(13), for the model beam consisting of $N_m = 4$ elemental beams (Fig. 4a) exhibits multiplicity equal to $N_m - 1 = 3$. This value is exactly equal to the number of degrees of freedom of the system. The analysis presented here can be generalized to hierarchical beams comprising an arbitrary number of elemental beams. It is then straightforward to show that the multiplicity of the roots of the characteristic bifurcation equation, i.e. Eq.(13), will be $N_m - 1$ for any N_m in $\mathbb{N}$. This implies, in turn, that we will obtain $n = N_m - 1$ buckling modes with identical critical loads. For illustration purposes, in Figs. 4b-d we show the $n = 1, 2, 3$ buckling modes for the hierarchical beam in Fig. 4a. The latter are drawn qualitatively. We emphasize here that Eq. (13), which in turn results from solving the stability equation, i.e. Eq. (12), is a necessary result for obtaining the bifurcation scenario depicted in Fig. 4. The analytical findings here presented are corroborated by the full-scale FE eigenvalue analysis of Section 3.

3. Numerical bifurcation analysis

This section deals with the full-scale FE bifurcation analysis of the hierarchical beams in Fig. 1c subjected to a uniaxial compressive loading. The study is conducted using the commercial FE solver ABAQUS/Standard. We obtain the critical loads (eigenvalues) and the corresponding buckling modes (eigenvectors) of the structures via a linear perturbation procedure (*BUCKLE analysis). Throughout the numerical study, we employ 2D geometries and model the material as a linear elastic solid with Young's modulus $E = 3.6$ MPa and Poisson's ratio $\nu = 0.49999$. The values of such parameters correspond to those of the rubber-like material used in the experiments. In particular, we generate structured meshes using linear hybrid (for incompressibility) plain-strain elements (i.e. ABAQUS element CPE4H) and apply the same boundary conditions as in the experiments. Specifically, the bottom edge is fixed in both the vertical and horizontal directions (i.e. encastre constraint), whereas the top edge is fixed in the horizontal direction to prevent both its lateral displacement and its rotation. A uniform axial compression is then applied at the model's top edge through a reference node (Hibbitt et al., 1998).

3.1. Hierarchical vs. non-hierarchical beam buckling

In order to set the problem, we first compare the bifurcation response of a representative hierarchical beam (see Fig. 1c-top), with that of a homogeneous beam of equal macroscopic slenderness.

Specifically, we consider a hierarchical beam assembled with $N_m = 4$ elemental modules, where every module has length 30 mm and width 10 mm. The physical dimensions of the module correspond to those used in the experiments. Each module, in turn, comprises four elemental beams of length 25 mm and width 1.25 mm. Henceforth, we define the elemental beam slenderness, denoted as λ, as the ratio of its length to its width. Moreover, we use $P_{cr\mathbf{n}}$ to denote the n^{th} critical load, with the lowest predicted eigenvalue being P_{cr1}.

The FE bifurcation analysis of the 4-module hierarchical system, consisting of elemental beams of slenderness $\lambda = 20$, reveals that the first three eigenvalues have nearly the same magnitude, whereby the amplitude of the subsequent ones is much higher and thus not shown in the following. Notably, the obtained values are $P_{cr2} \approx 1.003 P_{cr1}$ and $P_{cr3} \approx 1.027 P_{cr1}$. Fig. 5(top) shows the corresponding buckled patterns of the analyzed hierarchical system. As seen, the eigenmodes associated to P_{cr1}, P_{cr2} and P_{cr3} describe undulated patterns that resemble closely the eigenmodes displayed in the canonical Euler buckling problem. These modes are depicted in Fig. 5 (bottom). However, and in stark contrast with this hierarchical counterpart, a homogeneous beam has eigenvalues that are far apart. In particular, higher-order buckling modes with half-wavelength $n = 2$ and $n = 3$ correspond for the homogeneous beam to eigenvalues $P_{cr2} = 4P_{cr1}$ and $P_{cr3} = 9P_{cr1}$ respectively. The latter are therefore n^2-times higher than P_{cr1}, where the lowest eigenvalue for a fixed-ends beam of length l is $P_{cr1} = 4\pi^2 EI/l^2$.

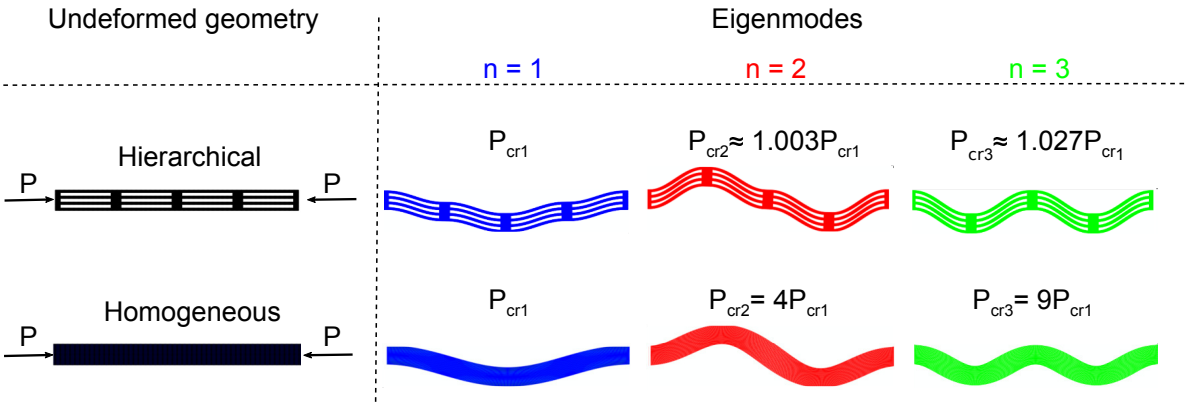

Figure 5: Hierachical *vs.* non-hierarchical beam buckling under axial compression. (top) FE results showing the first three eigenmodes and the associated eigenvalues of a hierarchical beam assembled with $N_m = 4$ modules. Every module in turn consists of four elemental beams of slenderness $\lambda = 20$. The deformation patterns of the hierarchical beam resemble closely the modes obtained in the canonical buckling problem of a homogeneous beam with identical macro-scale slenderness (bottom). In contrast with buckling of a homogeneous beam, such modes are associated to eigenvalues of nearly equal amplitude.

The findings of this numerical case study corroborate the analytical results obtained in Section 2.3. More interestingly, our results show that introducing hierarchy into a simple beam allows to bring the first three eigenvalues very close and thus unravels a novel route to achieve in practice higher order Euler buckling modes. In the sequel, we present a systematic investigation of the bifurcation of a large number of hierarchical beams (Section 3.2) and then use these results to explore, both experimentally and numerically, the post-bifurcation regime (Section 4). Notably, we rely on the results of the numerical bifurcation study to fabricate the test samples via 3D-printing as well as to guide experiments (Section 4).

3.2. Bifurcation loads and eigenmodes

In this section, we explore systematically the effect of two main geometrical parameters, namely the slenderness of the 2$^{\text{nd}}$-order macroscopic beam and the slenderness λ of the 0$^{\text{th}}$-order elemental beam. The slenderness of the macroscopic beam is parameterized by the number N_m of the elemental modules, which have fixed dimensions. Therefore, in order to vary the slenderness λ of the elemental beam, we decrease its width and keep its length constant. In the interest of making the parametric study tractable in this section, every module comprises four elemental beams (see Fig. 5(top)).

We first assemble four groups of modules using elemental beams with increasing slenderness (or aspect ratio) $\lambda = 12.5, 15.6, 20, 50$. Subsequently, for each module geometry, we generate numerically several hierarchical structures by increasing the number of modules from $N_m = 2$ to $N_m = 12$. We note in passing that, due to the limitations of the maximum build volume ($25 \times 25 \times 20\text{cm}^3$) of our 3D printer, we can only explore experimentally structures with $N_m \leq 8$ modules and elemental beams of slenderness $\lambda \leq 25$.

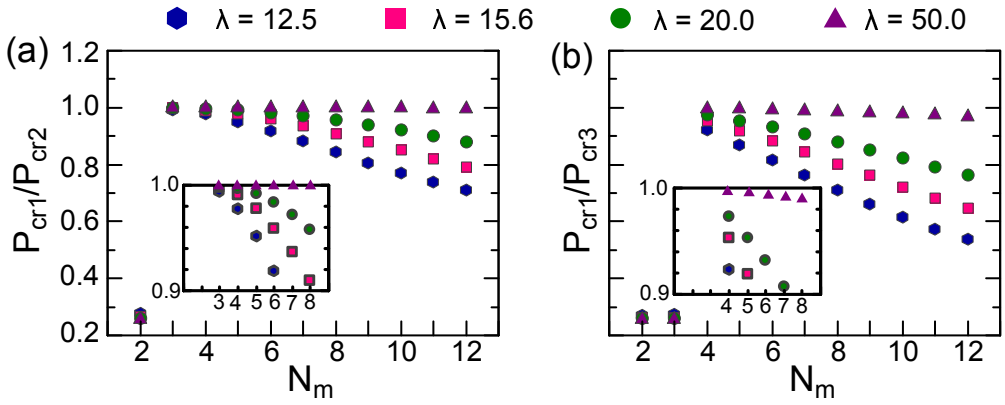

Figure 6: Results of the numerical bifurcation analysis onto various hierarchical beams under axial compression. Normalized critical loads (a) P_{cr1}/P_{cr2} and (b) P_{cr1}/P_{cr3} as a function of the number of modules N_m. Results denoted by identical symbols consist of elemental beams of the same slenderness λ.

Results of the bifurcation analysis are reported in Figs. 6a and 6b. Therein, we plot the ratio P_{cr1}/P_{cr2} (Fig. 6a) and P_{cr1}/P_{cr3} (Fig. 6b) as a function of the number of modules N_m. For most of the structures simulated, the results indicate that the three lowest eigenvalues are very close. Notably, the ratios P_{cr1}/P_{cr2} and P_{cr1}/P_{cr3} diverge gradually from unity with the increase of the macroscale beam slenderness (i.e with the increase of N_m) as well as with the decrease of the elemental beam slenderness λ. The only exception is observed for $N_m = 2$ in Fig. 6a,b where the eigenvalues are well far apart and for $N_m = 3$ in Fig. 6b, where only P_{cr1}/P_{cr3} is very different from unity. For completeness, we show in Fig. 7 the corresponding eigenmodes for a number of selected hierarchical beams consisting of $N_m = 3, 4, 6, 8$ modules and elemental beams with slenderness $\lambda = 20$. Collectively, the results in Figs. 6 and 7 imply that one possible strategy to achieve experimentally higher-order buckling modes is via compressive deformation of hierarchical beams with $P_{cr1}/P_{cr2,cr3}$ as close to unity as possible.

The observed deviation from unity of P_{cr1}/P_{cr2} and P_{cr1}/P_{cr3} with the increase of N_m (Fig. 6), can be rationalized on account of the competition between microscopic buckling of the elemental beams and macroscopic buckling of the hierarchical structure. In particular, by increasing the slenderness of the hierarchical beam (i.e. by increasing N_m), macroscopic buckling may occur at loads lower than the critical buckling load of the elemental beams. Our interpretation is consistent

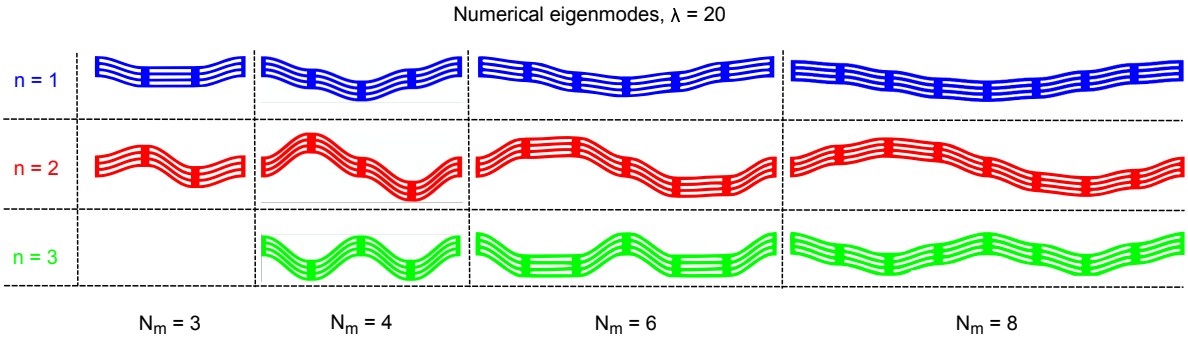

Figure 7: Numerical eigenmodes obtained from the numerical bifurcation analysis onto hierarchical beams with $\lambda = 20$ and $N_m = 3, 4, 6, 8$. The predicted eigenmodes correspond to the eigenvalues in Fig. 6 for the same geometrical parameters.

with an earlier study by Ohno et al. (2004) on the buckling of square honeycombs. Using a two-scale theory of updated Lagrangian type, the authors showed that the very-long-wave buckling of an elastic square grid occurs past the onset of macroscopic instability if the periodic length is sufficiently long. In this light, we can explain the results of Fig. 6. We focus for instance on beams assembled with elemental beams of slenderness $\lambda = 20$. As long as the hierarchical beam slenderness is small, i.e. $3 \leq N_m \leq 5$, the elemental beam buckles first. Since the latter now controls the bifurcation response of the entire structure, the critical load ratios $P_{cr1}/P_{cr2,cr3}$ are closer to unity, see also the results of Section 2. In turn, for intermediate values of the hierarchical beam slenderness, i.e. $5 \leq N_m \leq 8$, the 2^{nd}-order beam itself also tends to buckle as a whole thus introducing a non-trivial coupling between the two scales. This coupling leads to the gradual decrease of the critical load ratios $P_{cr1}/P_{cr2,cr3}$. Subsequently, as the hierarchical beam becomes even more slender ($N_m > 8$), it starts behaving as a classical, albeit non-homogeneous, Euler beam with $P_{cr1} << P_{cr2} << P_{cr3}$. Therefore, by increasing the slenderness of the elemental beam, one should expect microscopic buckling to win over macroscopic buckling in a large number of cases. We validate further this observation, by including results for very slender elemental beams, i.e. $\lambda = 50$. In this case, the critical load ratios remain very close to unity even up to $N_m = 12$. Note however that the absolute value for P_{cr1} becomes very small since $\lim_{\lambda \to \infty} P_{cr1} = 0$, thus making both the fabrication and testing of such structures not possible in the present study.

4. Experimental and numerical study of the post-bifurcation response

In this section, we use the results of the numerical bifurcation analysis to study the post-bifurcation response of the hierarchical beams both experimentally and numerically. Specifically, the predicted numerical eigenmodes (see e.g. Fig. 7) are introduced as geometrical imperfections of small amplitude both in the 3D-printed test samples and in the numerical models for the finite-strain analysis of the post-bifurcation response. Our goal is to explore whether the first three modes of buckling in a hierarchical beam (see e.g. Fig. 5) can be obtained experimentally and numerically at finite strains. In the following, we describe a road-map to to achieve this goal.

4.1. Experimental Methods

For our experiments, we 3D-print test samples assembled with elemental beams of slenderness $\lambda = 10, 20, 25$. Due to the constraints imposed by our 3D-printer (Stratasys EDEN 260 VS, with build volume of $25 \times 25 \times 20\text{cm}^3$), we use elemental beams of length equal to 25 mm, while the

modules have length 30 mm and width 10 mm. This further leads to a homogeneous spacing between the elemental beams of thickness equal to 5 mm (see Fig. 1c). Hence, $\lambda = 10, 20, 25$ correspond to elemental beams of thickness equal to 2.5 , 1.25 and 1 mm respectively. This value, i.e. 1 mm, corresponds to the minimum thickness that can be 3D-printed with sufficient accuracy when samples are fabricated out of soft rubber-like material.

In order to achieve higher-order buckling modes in a real experiment, we harness the numerically-designed imperfection sensitivity of the hierarchical beams to trigger selectively the buckling patterns. Before discussing in detail this part, it is important to mention that the problem of mode-interaction and imperfection sensitivity has been extensively studied in mechanics. When a structural system displays interactive effects between modes, it may exhibit imperfection-sensitivity. Systems of this type are many and examples include thin spherical shells under external pressure (Karman, 1939), stiffened panels (Koiter and Pignataro, 1976), thin-wall (Thompson and Lewis, 1972) and reticulated columns (Thompson and Hunt, 1973), as well as wide-flanged beams (Van der Neut, 1969) and sandwich structures (Hunt et al., 1988). A comprehensive historical survey on the matter can be found in Hunt (1986).

In the present study, we introduce the geometrical imperfection in the test specimen following a numerically-aided experimental protocol. Two other recent examples of the fabrication of thin structures with a precisely-engineered defect are given in Lee et al. (2016); Marthelot et al. (2017). We first create *imperfect* geometries using the *IMPERFECTION option in ABAQUS. This command enables us to modulate node-by-node the 2D mesh of the hierarchical beams with small-amplitude perturbations. These perturbations have the computed geometry of the $n = 1, 2$ and 3 eigenmodes that correspond to the eigenvalues P_{cr1}, P_{cr2} and P_{cr3}, respectively, shown in Fig. 7. Henceforth, we denote each eigenmode-like imperfection as $n = 1, 2, 3$ for consistency with the FE bifurcation analysis. The nodal perturbation amplitude is set equal to 5% of the total width of the module, i.e. 500 μm. We note in passing that this value is in the order of the dimensional accuracy of our 3D-printer. The *imperfect* test samples are then realized by first extruding the 2D *imperfect* models into 3D solids of out-of-plane thickness 10 mm, and then by fabricating them via high-precision 3D-printing. The specimens are manufactured out of a soft rubber-like material (commercial name TangoBlack FLX 930).

Subsequently, we perform uniaxial compression experiments and track the shape evolution of the samples with a CCD camera. The experiments are carried out under displacement control (i.e. hard device) with a constant rate of $10^{-3}mm/s$ and are interrupted at a nominal strain of $\varepsilon = -u/\mathcal{L} = 0.06$. Here, u denotes the recorded displacement signal and $\mathcal{L}$ the initial specimen's length. We measure the axial force with the aid of a 10 N load transducer (Futek LPM200) which has an accuracy of 10^{-3}N. We also note that the applied compression rate is slow enough to ensure quasi-static strain-rates, i.e., $10^{-5}s^{-1}$ and $4 \cdot 10^{-6}s^{-1}$ for the shortest ($N_m = 3$) and longest ($N_m = 8$) structures respectively. In parallel with the experiments, we carry out finite plain-strain FE simulations using the same *imperfect* geometries as the test specimens. We use the numerical results to probe the experimental (nominal) stress-strain response as well as the resulting post-bifurcation patterns. For consistency with experiments, we apply clamped boundary conditions and model the polymer as a nearly incompressible neo-Hookean solid with Young's modulus $E = 3.6$ MPa and Poisson's ratio $\nu = 0.49999$ (Wang et al., 2011).

4.2. Overall stress-strain response and higher-order modes

In this section, we present the experimental and numerical results of the post-bifurcation response of various selected hierarchical beams. We first focus on structures comprising elemental

beams of slenderness $\lambda = 20$ and assembled with $N_m = 3, 4, 6, 8$ modules. In Fig. 8a, we report the nominal overall stress-strain response of these structures. Overall, the data show a very good quantitative agreement between experiments and simulations. Moreover, the data collectively indicate that the response of all structures is characterized by a nearly linear elastic initial response with a departure from linearity that coincides with the onset of buckling. The latter, in turn, occurs at very low nominal strains, namely well below 0.01 strain.

On the other hand, the post-bifurcation response is highly dependent on N_m. Specifically, we find that hierarchical beams with $N_m = 6, 8$ modules exhibit significant softening early after the onset of bifurcation. This is observed both experimentally and numerically. By contrast, systems with smaller macroscopic slenderness, i.e. with $N_m = 3, 4$, exhibit in all cases but one a stiffening post-bifurcation response. The only exception is observed for the $N_m = 4$-module system with an eigenmode-like imperfection of type $n = 1$ (see Fig.7a), which displays an initial plateau region evolving to a very weak softening at higher strains.

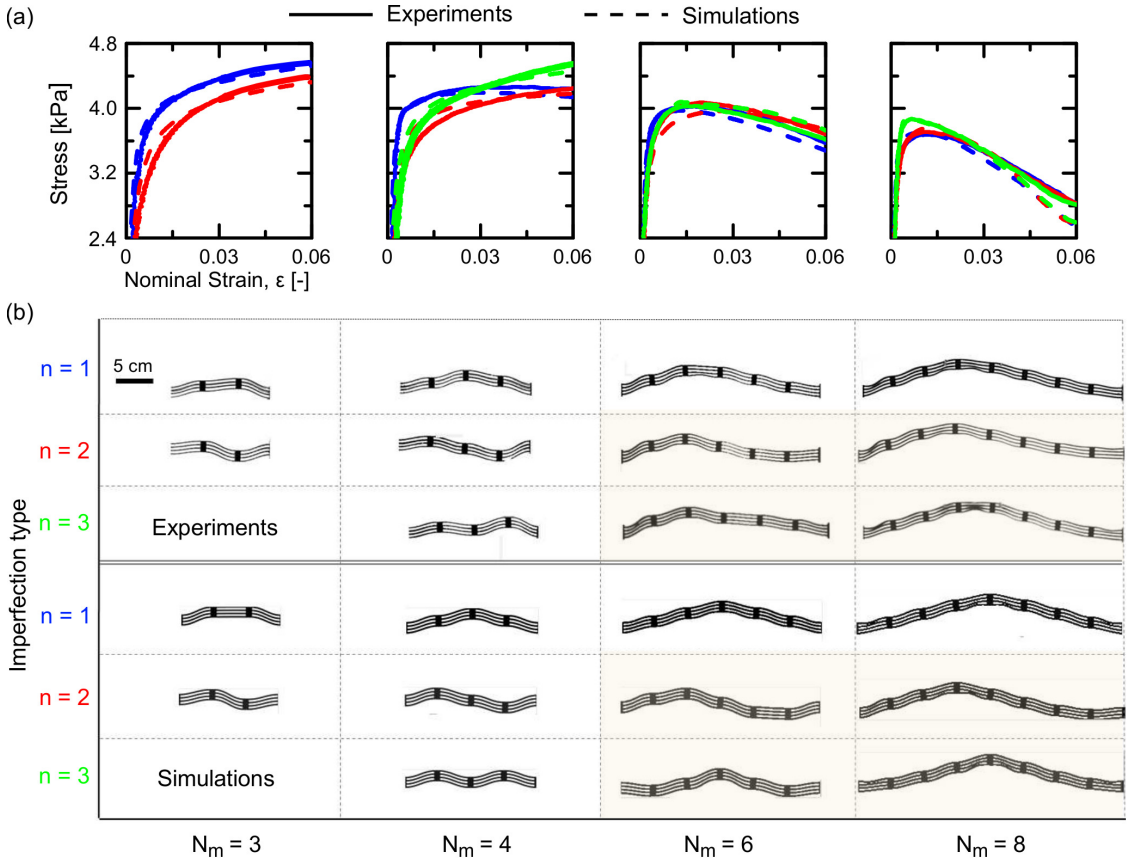

Figure 8: Post-bifurcation response of various hierarchical beams comprised of elemental beams with slenderness $\lambda = 20$ and $N_m = 3, 4, 6, 8$. (a) Experimental (solid lines) and numerical (dashed lines) nominal stress-strain response. The colors blue, red and green correspond to imperfection-type $n = 1$, 2 and 3 respectively. (b) Experimental (top row) and numerical (bottom row) post-bifurcation patterns at 0.03 nominal strain. The light yellow area comprises all hierarchical systems whose deformation patterns do not correspond to the initial eigenmode-like imperfection.

In Fig. 8b, we show the experimental (top row) and numerical (bottom row) post-bifurcation patterns at 0.03 nominal strain. Here too, there is a good qualitative agreement between experiments and simulations. Interestingly, we find that higher-order buckling modes can be achieved

experimentally and persist deep into the post-bifurcation regime. More specifically, we observe that the buckled patterns of samples with $N_m = 3, 4$ modules maintain the sample's imperfection profile. This is depicted in Fig. 7 for the same geometrical parameters and is obtained from the FE bifurcation analysis. To the best knowledge of the authors, this is the first time that such modes are obtained experimentally using a plane beam geometry.

On the other hand, we find that higher-order modes do not emerge in longer hierarchical beams, i.e., $N_m = 6, 8$. The deformation patterns of these systems are highlighted with light yellow background in Fig. 8b. As N_m and thus the macroscopic beam slenderness increases, the interaction between the two structural scales emerge. This interaction promotes the combination of gradually increasing modes and eventually leads to localized deformation patterns (Tvergaard and Needleman, 1980; Hunt and Wadee, 1998). For example, the hierarchical beam with $N_m = 6$ and an initial $n = 2$-type imperfection (Fig. 7) clearly displays combined geometrical features of both the $n = 1$ and $n = 2$ eigenmodes. The analysis of the deformation patterns, becomes less and less trivial as N_m increases further. In particular, the patterns of all 8-module beams diverge significantly from the initially assigned eigenmode profile. For instance, one can compare Fig. 7 with Fig. 8b for $N_m = 8$. For these systems, patterns also involve contact between adjacent elemental beams and may result from infinite local modes (Byskov, 1987). We examine the pattern evolution leading to localization as well as the transition to discontinuous buckling in Section 5.

Next, we probe the ability to trigger selectively high-order buckling modes when the slenderness λ of the elemental beams is varied in hierarchical beams with constant macroscopic slenderness (i.e. constant N_m). Specifically, we compare the post-bifurcation response as well as the deformation patterns of hierarchical systems comprised of $N_m = 4$ modules and assembled with elemental beams of either $\lambda = 10$ and $\lambda = 25$. Results are reported in Fig. 9.

Fig. 9 reveals that all $N_m = 4$ beams explored retain the capability of achieving higher-order buckling modes irrespective of the slenderness λ of the elemental beams. We observe that higher-order buckled patterns remain stable when the nominal strain increases from 0.03 to 0.04. The only exception is found for the system with $\lambda = 10$ and an initial imperfection of type $n = 3$. In this case, the deformation pattern exhibits localization at the middle section of the hierarchical beam. In parallel, the corresponding stress-strain response of this system (see green curves in Fig. 9a) reaches a maximum deep into the post-bifurcation regime (i.e past 0.03 strain). This response is captured by both experiments and numerical simulations, albeit a difference is observed after the maximum is reached in this case.

We conclude this section by noting that the FE numerical calculations prove to be very accurate both qualitatively and quantitatively. Not only they are able to predict by comparison to experiments extremely well the overall stress-strain response but also the obtained patterns even when those reach a more localized type of deformation. It is noted that no particular imperfections, apart from the pre-assigned eigenmode imperfection necessary to trigger experimentally and numerically the designed buckling mode, are needed in the FE simulations to recover the localized patterns. This strongly indicates that the application of standard (Dirichlet and Neumann in this case) boundary conditions (and not periodic ones) to the boundary value problem are capable of retaining the necessary features of the observed localized deformation.

4.3. Additional numerical results for $\lambda = 50$

For completeness, in this section we explore numerically hierarchical beams assembled with very slender elemental beams. As anticipated earlier, large values of the slenderness λ of the elemental beam cannot be attained experimentally due to technical constraints. In an attempt to gain further

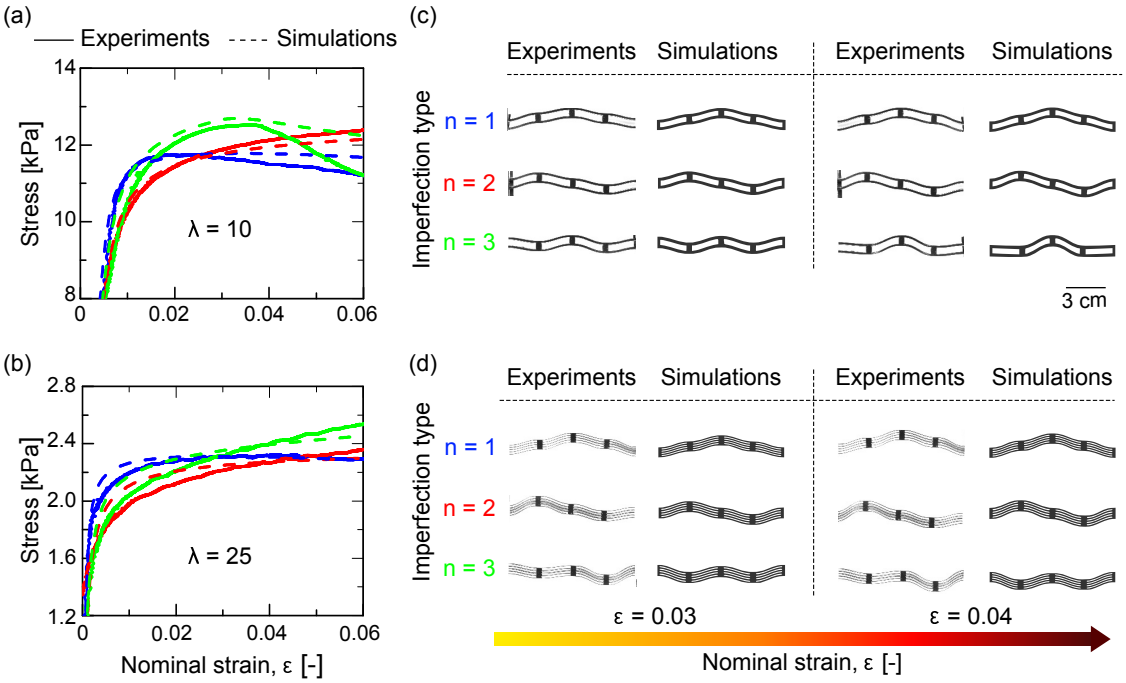

Figure 9: Post-bifurcation response of $N_m = 4$-module hierarchical systems comprising of elemental beams with slenderness $\lambda = 10, 25$. (a)-(b) Experimental (solid lines) and numerical (dashed lines) nominal stress-strain response. The colors blue, red and green correspond to imperfection-type $n = 1$, 2 and 3 respectively. (c)-(d) Experimental and numerical post-bifurcation patterns at 0.03 and 0.04 nominal strain. (a),(c) and (b),(d) correspond to systems with $\lambda = 10$ and $\lambda = 25$ respectively.

understanding in this regime, we use FE simulations to investigate the post-bifurcation response of structures comprised of $N_m \leq 12$ modules and elemental beams with $\lambda = 50$. Specifically, our goal is to show that, by increasing λ, one can achieve higher-order buckling modes in beams with a larger number of modules N_m. In the interest of comparing results with those presented in Fig. 8, we focus on hierarchical beams assembled with $N_m = 4, 6, 8, 10$ and 12 modules.

In Fig. 10, we report the results of the simulated hierarchical beams constructed with very slender elemental beams, i.e. $\lambda = 50$. For consistency with Fig. 8, we show in Fig. 10a the nominal stress-strain response and in Fig. 10b the corresponding post-bifurcations patterns at 0.03 nominal strain.

By comparing Fig. 10 with Fig. 8, we find that increasing the slenderness of the macroscale beam (i.e. increasing N_m) leads to softening (i.e. discontinuous buckling) in the post-bifurcation regime. More interestingly, all beams (i.e. $N_m = 4 - 12$) with pre-assigned eigenmode types $n = 1, 2$ maintain faithfully the original eigemode-like pattern in the post-bifurcation regime. This is also true for the third eigenmode but only for $N_m = 4$. Instead, beyond $N_m \geq 6$, the hierarchical beams with $n = 3$ exhibit localized deformation patterns as shown in the highlighted yellow region in Fig. 10b. This localization is more pronounced for $\lambda = 50$ than for $\lambda = 20$ observed in Fig. 8.

It is well established that localized buckled patterns in composite columns result from the interaction between buckling modes with different wavelength (Hunt and Wadee, 1998). Interactive buckling leads to an unstable post-bifurcation response and corresponds, if the system contained no imperfection, to a secondary bifurcation point of the post-bifurcation path of the triggering mode, i.e. the mode with the lowest critical load (see for instance Okumura et al. (2004)). In realistic

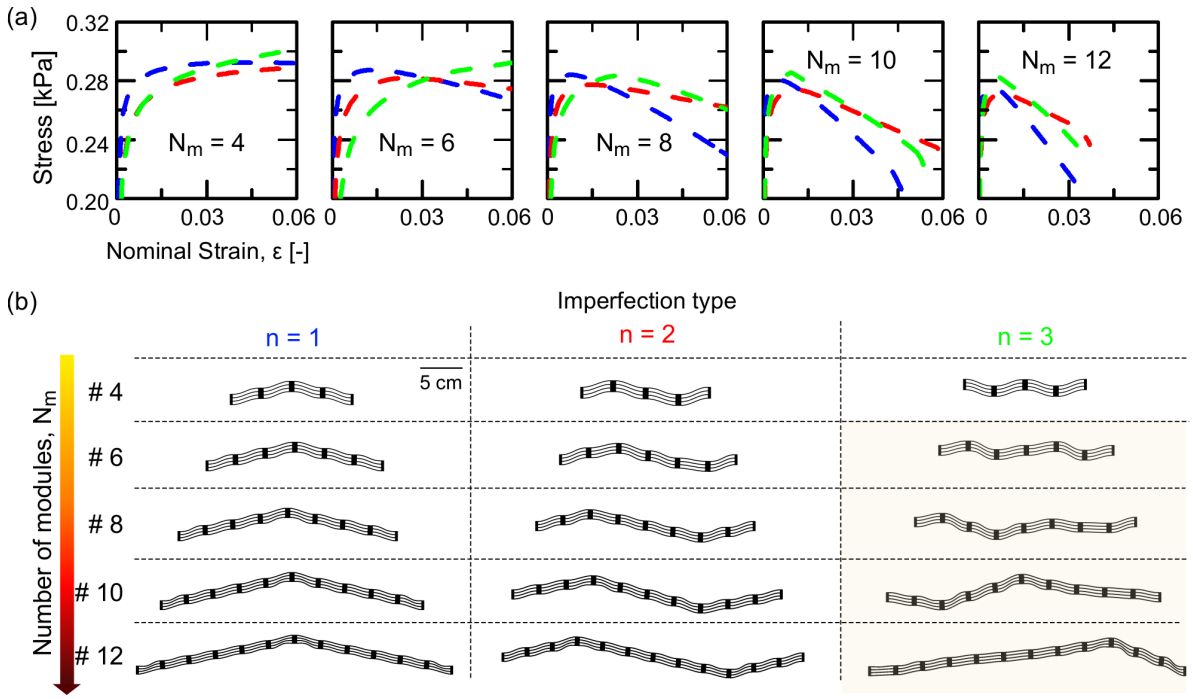

Figure 10: Numerical post-bifurcation response of various hierarchical beams comprised of elemental beams with slenderness $\lambda = 50$ and $N_m = 4, 6, 8, 10, 12$. (a) Nominal stress-strain response (the colors blue, red and green correspond to imperfection-type $n = 1$, 2 and 3 respectively) and (b) post-bifurcation patterns at 0.03 nominal strain. The highlighted yellow area comprises all hierarchical systems whose deformation patterns do not correspond to the initial eigenmode-like imperfection.

(imperfect) systems however, the equilibrium path displays a single bifurcation point that still bears the hallmarks of a pitchfork bifurcation problem, see e.g. the work by (Yiatros and Wadee, 2010) on sandwich struts and by (Barbero et al., 2000) on intermediate-length in thin-walled columns. The onset of interactive buckling, and thus the point of secondary bifurcation, can be quantified by tracking the evolution of the different buckling modes amplitudes. Such an analysis is not trivial for the proposed hierarchical beams due to the large number of kinematic variables that can be reported. Here, we study numerically the onset of interactive buckling on systems with $n = 3$, as these exhibit deformation patterns that highly diverge from their eigenmode-like imperfection (see Fig. 10b). For a number of selected structures in Fig. 10 (i.e. $N_m = 6, 8, 10$), we examine the evolution of the displacement at the midspan of the hierarchical beam. Such a kinematic variable is chosen for simplicity, yet it yields meaningful observations. The displacement amplitude is normalized by the specimen's width (i.e. 10 mm) and is denoted by w^*. Corresponding stress-strain and w^* results are reported in Fig. 11 as a function of the applied axial strain.

Figure 11 clearly shows the onset of interactive buckling and thus indicates a secondary bifurcation along the buckled equibilibrium path. Interestingly, where the response of the hierarchical beam exhibits a max stress point, and in turn softening, the normalized displacement amplitude at midspan, w^*, becomes non-zero and increases monotonically with the overall applied axial strain, see curves for $N_m = 6, 8$. By contrast, when the post-bifurcation response displays no softening (i.e. system with $N_m = 6$), w^* remains practically zero during the entire deformation history. Since secondary bifurcation leads to localization (Tvergaard and Needleman, 1980), the post-bifurcation patterns of the hierarchical beams, in Fig. 11 with $N_m = 6, 8$, exhibit mode coupling resulting

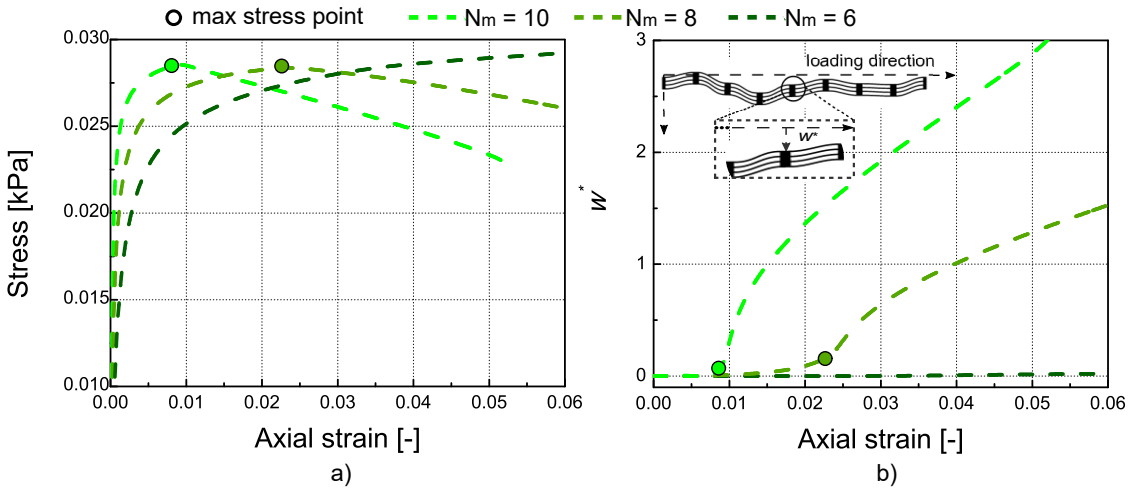

Figure 11: Numerical results for the effect of interactive buckling in selected hierarchical beams with $\lambda = 50$ and $N_m = 6, 8, 10$ and geometric imperfection $n = 3$. (a) Nominal stress-strain response, and (b) evolution of the normalized midspan displacement amplitude w^* (see the inset sketch for the definition of $w*$). The filled circles indicate the maximum stress point in (a), and the onset of interactive buckling and secondary bifurcation and localization in (b).

to complex patterns whereby the curvature of some elemental beams localizes, see Fig. 10. This curvature localization, discussed in more detail in the following section, leads to morphological patterns that resemble the *crinkling* patterns observed in graphene Kothari et al. (2018) and in magnetorheological polymer film/substrate blocks Psarra et al. (2017).

5. Discussion on curvature localization in hierarchical systems

Buckling in the hierarchical beams of this study leads to the emergence of higher-order buckling modes but also to localized post-bifurcation patterns and negative stress-strain response beyond the onset of bifurcation. The scope of this section is to examine in more detail the localization response using mainly the FE numerical results. In this regard, we focus on hierarchical beams with an eigenmode-like imperfection of type $n = 1$. The conclusions are similar for $n = 2$ and $n = 3$ and thus are not discussed here.

In Fig. 12a, we compare the stress-strain response of hierarchical beams with $n = 1$ eigenmode-type imperfection and $N_m = 3, 4, 6, 8$ modules (see blue curves in Fig. 8a). With increasing slenderness of the macroscale beam (i.e. increasing N_m), we observe a gradual transition from a positive to a negative slope of the stress-strain response. Consequently, the stress-strain response is characterized by the presence of a maximum (i.e. limit load) when strong softening is observed (see for example beams with $N_m = 6$ and $N_m = 8$). The strain at which the maximum stress is reached is higher than the critical strain at which buckling sets in, except for $N_m = 8$ that the limit load appears early after bifurcation.

To examine further the transition from hardening (i.e. positive slope) to softening (i.e. negative slope) response, we consider the two most representative cases comprised of respectively $N_m = 4$ and $N_m = 8$ modules. In Figs. 12b-c, we report both the experimental and numerical deformation patterns at increasing values of strain. Overall, the present simulations are in very good quantitative agreement with the experiments. Contrary to the $N_m = 4$ beam, the $N_m = 8$ beam exhibits

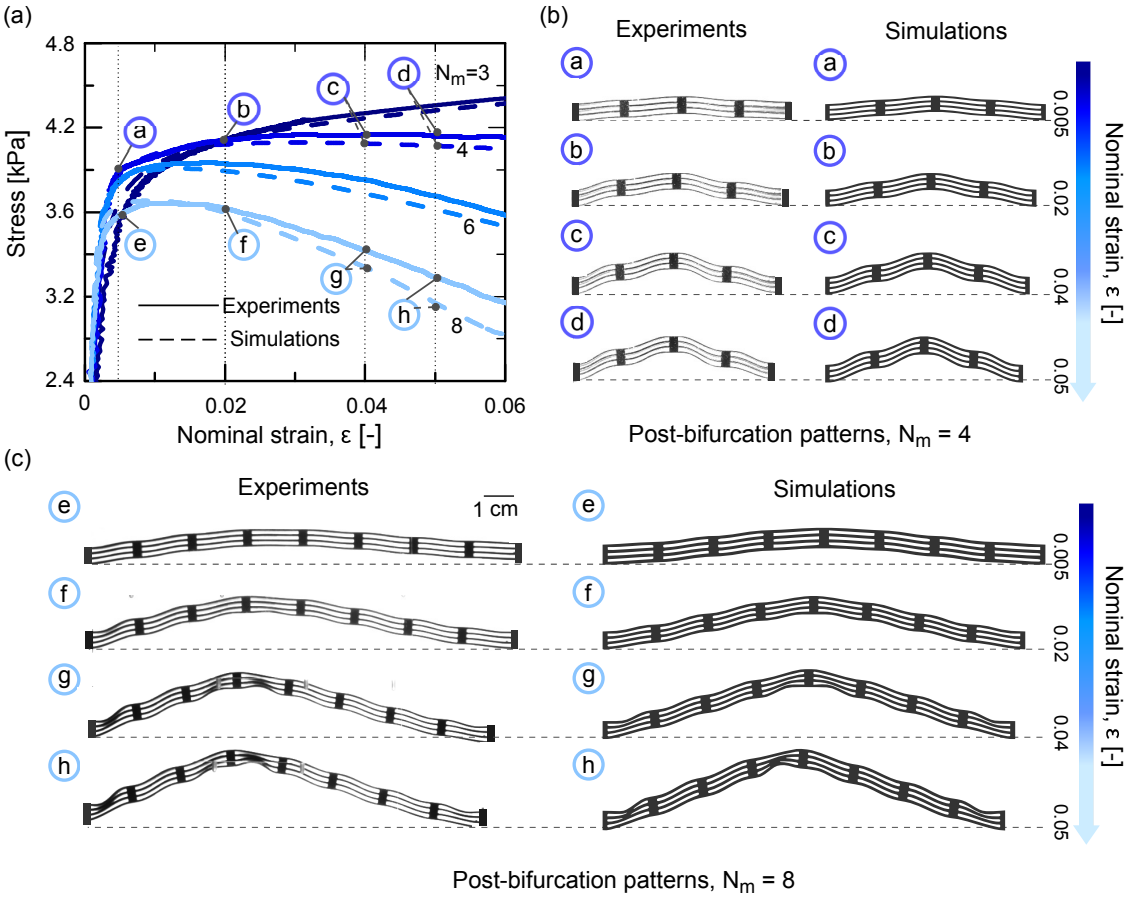

Figure 12: (a) Comparison of post-bifurcation stress-strain response of hierarchical beams with $\lambda = 20$ and $N_m = 3, 4, 6, 8$. All beams contain an imperfection of eigemode type $n = 1$ and correspond to curves in blue color in Fig. 8a. Experimental and numerical results are denoted with solid and dashed lines respectively. (b)-(c) Evolution of the experimental and numerical post-bifurcation patterns at increasing values of strain for the two most representative cases, i.e. $N = 4$ and $N_m = 8$.

localized post-bifurcation patterns. Moreover, localization becomes more and more pronounced as deformation increases leading eventually to the contact between neighbouring elemental beams. The fact that a negative stress-strain response is associated with highly localized deformation patterns suggests that the interactive effects between modes and scales is very strong. Our findings are consistent with the well-known study by Tvergaard and Needleman (1980), who showed theoretically that structures exhibiting a limit load and softening lead to localized buckling patterns that differ from their lower-order periodic buckling eigenmodes and *vice versa*.

Such localized deformation patterns are often observed in many other cellular structures. Notable examples include the regular hexagonal honeycombs (Papka and Kyriakides, 1998, 1994) as well as the holey periodic elastomers under in-plane compression (Triantafyllidis et al., 2006; Mullin et al., 2007). The mechanisms that lead to localized buckling modes have been analyzed theoretically using simplified models on elastic foundations (Tvergaard and Needleman, 1980; Audoly, 2011; Hunt et al., 1988) . The pilot study by Hunt et al. (1988) of a simplified sandwich panel comprising two thin flanges separated by a Winkler-type core can qualitatively predict such features. However, it relies on two "pre-assumed" buckling modes that may not prove sufficient to

described the more complex scenario of our hierarchical beams, as will be shown next. Notably, it cannot capture the localization of the buckled pattern that is found to be more prominent in some elemental beams, as shown in Fig. 12b.

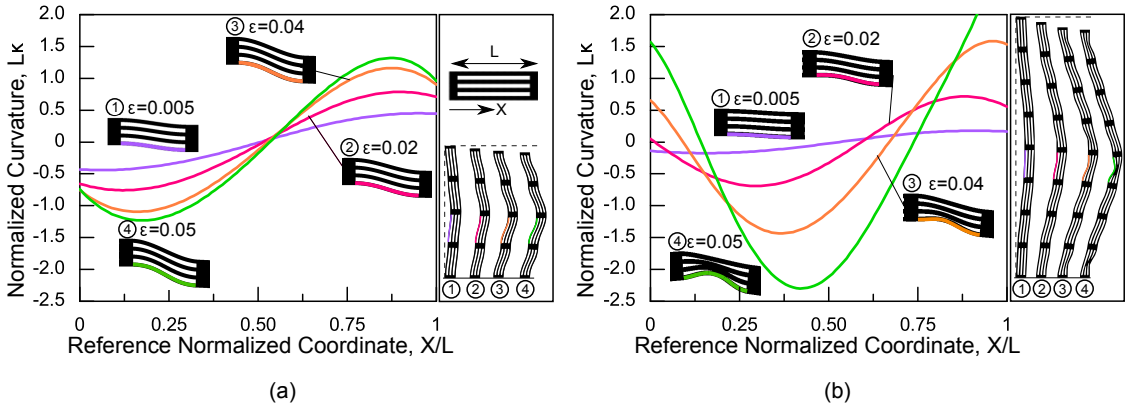

Figure 13: Curvature localization in the hierarchical beams of Fig. 12b and comprised of (a) $N_m = 4$ and (b) $N_m = 8$ modules respectively. Plots of the normalized curvature $L\,\kappa$ as a function of the reference normalized coordinate X/L (see inset) are reported for a selected elemental beam whose profile is extracted from the numerical deformation patterns. For each system, the selected beam is highlighted using coloured lines.

In order to quantify the localization effect, we compute the evolution of the normalized curvature, $L\,\kappa$, of one representative single elemental beam (highlighted in Figs. 13a,b) as a function of the reference normalized coordinate X/L. As seen, for the system with $N_m = 8$ (Fig. 13b) the normalized curvature of the single beam becomes markedly non-sinusoidal and localizes with increasing compressive strain ε. In contrast, for the system with $N_m = 4$ (Fig. 12b), the normalized curvature of the highlighted elemental beam remains well described by a sinusoid and only localizes, albeit weakly, at much larger strains. This very weak localization can be identified by noting the increase of the maximum point ($X/L \sim 0.82$) but not of the edge point ($X/L \sim 1$) when comparing the corresponding curves for $\varepsilon = 0.04$ and $\varepsilon = 0.05$ in Fig. 12a. This quantitative analysis explains the very weak softening of the $N_m = 4$-module beam at large strains (see Fig. 12a). It is also interesting to note that the profile of the localized beams evolves gradually and continuously with increasing applied load. In addition, the curvature localization evolution varies for all elemental beams constituting the module as a result of the highly heterogeneous deformation fields in the hierarchical beam. It thus seems too complex in the present case to capture the two-scale profiles (i.e. that of the elemental beams and that of the hierarchical macroscopic beam) with a small number of sinusoidal modes or even combination of elementary functions. Finally, we note that the observed overall buckled patterns of the hierarchical beams in Fig.12c resemble remarkably the crinkle morphology Pipkin (1986) observed in graphene (Kothari et al., 2018) and magnetorheological polymer film/substrate blocks (Psarra et al., 2017).

6. Concluding remarks

In this work, we propose a novel class of hierarchical beams that lead to higher-order Euler buckling modes. The analyzed structures have a simple architecture where a self-similar module, consisting of several elemental beams set in parallel, is assembled length-wise to form a 2^{nd} order hierarchical beam. Our design approach is highly versatile and enables exploring a broad range

of geometrical parameters. The main feature of such hierarchical beams is the possibility of obtaining higher-order Euler buckling modes under uniaxial compression. Such modes are carefully pre-designed to occur at nearly the same overall critical load. In order to rationalize the underlying bifurcation response of the hierarchical systems, we first use the beam column method to study analytically the stability of a hierarchical "model" beam consisting of a line array of simple homogeneous elemental beams rigidly connected at their ends. The critical load of this assembly is found to be equal to that of its elemental struts when these are treated as side-swaying beams with fixed slopes (i.e zero rotation) at both ends.

In the interest of exploring these features in a realistic structure, we use FE simulations to solve the bifurcation (eigenvalue and eigenvector) problem of the 2^{nd} order hierarchical beam. The numerical findings corroborate the analytical results of the previously mentioned model beam. In particular, the FE model allows to design hierarchical beams whose first three critical buckling loads are relatively close. The corresponding eigenmodes are found to correspond to undulated patterns resembling closely the canonical buckling modes of homogeneous beams with identical macroscopic slenderness. Nonetheless, the latter are known to exhibit critical bifurcation loads that are very far apart and for that reason the second and third eigenmodes are never observed in practice. In the sequel, an extensive parametric study is carried out to examine the relative effect of the elemental beam slenderness (measured by λ) and of the hierarchical beam slenderness (measured by the number of assembled modules N_m). Therein, we find that increase of λ leads to the first three critical eigenvalues being very close to each other even for large N_m. This is easily understood by noting that at very large λ's the elemental beam controls the buckling response of the hierarchical beam. By contrast, as λ decreases and N_m increases the overall slenderness of the hierarchical beam dominates the buckling response. A non-trivial coupling of the buckling response at two scales (which cannot be separated) is thus obtained and harnessed to program patterns.

We show the existence of such higher-order modes in practice by 3D-printing and experimental testing of the aforementioned computer-designed hierarchical beams. Specifically, we harness the imperfection sensitivity of our structures by assigning the numerically obtained eigenmodes to the hierarchical beams. The test samples are fabricated with the aid of high-precision 3D-printing using a rubber-like material. The same imperfection is also introduced in the numerical geometries, which are subsequently analyzed using finite strains and nonlinear Neo-Hookean elasticity. Overall the numerical simulations are found to be in very good agreement with experiments, both qualitatively and quantitatively even well inside the post-bifurcation regime.

In particular, the post-bifurcation response of the hierarchical beams reveals an initial linear elastic response followed by a stiffening or softening response after buckling sets in. As expected by the bifurcation analysis, the post-bifurcation results show that higher-order buckling modes can be triggered selectively in our systems when microscopic (elemental beam) buckling wins over macroscopic (hierarchical beam) buckling. This is the case for hierarchical beams comprising a small number of elemental modules (e.g. $N_m = 3, 4$) and for an experimentally attainable elemental beam slenderness $\lambda \leq 25$. For such systems, higher-order modes are observed to be stable deep into the post-bifurcation regime exhibiting in most cases stress-strain hardening. To obtain higher-order modes for $N_m \geq 6$ (i.e. more slender hierarchical beams), a large slenderness of the elemental beam $\lambda > 30$ is required. In this view, we analyze hierarchical beams with $\lambda = 50$ numerically and show that higher-order modes are indeed realizable for $N_m \geq 6$.

In a large number of cases, the hierarchical beams exhibit overall softening of the stress-strain response, which gradually leads to microscopic and macroscopic curvature localization. In this

regard, using the FE calculations (which are in very close agreement with the corresponding experiments), we examine quantitatively the resulting curvature localization of the elemental beams. It is shown that the initially sinusoidal pattern of a single elemental beam evolves "gradually and continuously" to a complex localized pattern that cannot be analyzed with a small number of sinusoidal functions in the present case. It is worth mentioning that the agreement between the numerical and the experimental results is very good and does not require the use of any additional imperfection, except for the initial smooth imperfection needed to trigger the desired higher=order Euler-type eigenmode. Perhaps a remark that requires additional validation, but is indeed unquestionable in the present study, is that the resolution of a boundary value problem with imposed Dirichlet (and Neumann) boundary conditions is numerically rich enough to predict realistically the experimentally observed localized patterns without the need of additional local imperfections.

We conclude this work by noting that the proposed simple hierarchical beams provide a gateway to multimodal instability-induced patterns by use of their intriguing and *programmable* undulated morphologies. Such hierarchical structures can be used in a number of applications from functional surfaces to structural self-similar hierarchical materials (Wang and Zhao, 2016; Kochmann and Bertoldi, 2017). Furthermore, the response of the proposed hierarchical structures is highly scalable since it is mainly dominated by the inherent geometrical nonlinearities. Thus, the main idea of the present work can be extended *ad infinitum* to higher orders of hierarchy albeit with increasing level of complexity and scale coupling. In addition, the hardening stress-strain response obtained when higher-order modes are achieved (see the case of $\lambda = 20$, $N_m = 4$ and $n = 3$) could be of interest in the context of dynamic energy absorption Gaitanaros et al. (2012); Barnes et al. (2014); Gaitanaros and Kyriakides (2014). Finally, owing to their rich bifurcation scenarios and mode selectivity, the present findings are likely to be of interest in the mathematics community and encourage exploration of the bifurcation phenomena by group theory analysis (Golubitsky et al., 2012; Healey and Dharmavaram, 2017).

7. Acknowledgements

The authors would like to acknowledge support by the European Research Council (ERC) under the European Union Horizon 2020 research and innovation program (grant agreement No 636903).

References

Ajdari, A., Jahromi, B.H., Papadopoulos, J., Nayeb-Hashemi, H., Vaziri, A., 2012. Hierarchical honeycombs with tailorable properties. International Journal of Solids and Structures 49, 1413–1419.

Audoly, B., 2011. Localized buckling of a floating elastica. Physical Review E 84, 011605.

Audoly, B., Boudaoud, A., 2008. Buckling of a stiff film bound to a compliant substrate–part i:: Formulation, linear stability of cylindrical patterns, secondary bifurcations. J. Mech. Phys. Solids 56, 2401 – 2421.

Barbero, E.J., Dede, E.K., Jones, S., 2000. Experimental verification of buckling-mode interaction in intermediate-length composite columns. International journal of solids and structures 37, 3919–3934.

Barnes, A., Ravi-Chandar, K., Kyriakides, S., Gaitanaros, S., 2014. Dynamic crushing of aluminum foams: Part i – experiments. International Journal of Solids and Structures 51, 1631 – 1645.

Bazant, Z., Cedolin, L., 2010. Stability of structures: elastic, inelastic, fracture and damage theories. World Scientific.

Bažant, Z.P., Christensen, M., 1972. Long-wave extensional buckling of large regular frames. Journal of the Structural Division 98, 2269–2289.

Byskov, E., 1987. Elastic buckling with infinitely many local modes. Journal of Structural Mechanics 15, 413–435.

Cai, S., Breid, D., Crosby, A.J., Suo, Z., Hutchinson, J.W., 2011. Periodic patterns and energy states of buckled films on compliant substrates. Journal of the Mechanics and Physics of Solids 59, 1094–1114.

Camacho-Lopez, M., Finkelmann, H., Palffy-Muhoray, P., Shelley, M., 2004. Fast liquid-crystal elastomer swims into the dark. Nature materials 3, 307.

Chen, X., Hutchinson, J.W., 2004. Herringbone buckling patterns of compressed thin films on compliant substrates. Journal of applied mechanics 71, 597–603.

Combescure, C., Elliott, R.S., 2017. Hierarchical honeycomb material design and optimization: Beyond linearized behavior. International Journal of Solids and Structures 115, 161–169.

Combescure, C., Henry, P., Elliott, R.S., 2016. Post-bifurcation and stability of a finitely strained hexagonal honeycomb subjected to equi-biaxial in-plane loading. International Journal of Solids and Structures 88, 296–318.

Danas, K., Mukherjee, D., Haldar, K., Triantafyllidis, N., 2018. Bifurcation analysis of twisted liquid crystal bilayers. Journal of the Mechanics and Physics of Solids .

Danas, K., Triantafyllidis, N., 2014. Instability of a magnetoelastic layer resting on a non-magnetic substrate. J. Mech. Phys. Solids 69, 67 – 83.

Deshpande, V.S., Fleck, N.A., Ashby, M.F., 2001. Effective properties of the octet-truss lattice material. Journal of the Mechanics and Physics of Solids 49, 1747–1769.

Fan, H., Jin, F., Fang, D., 2008. Mechanical properties of hierarchical cellular materials. part i: Analysis. Composites Science and Technology 68, 3380–3387.

Fan, H., Jin, F., Fang, D., 2009. Uniaxial local buckling strength of periodic lattice composites. Materials & Design 30, 4136–4145.

Gaitanaros, S., Kyriakides, S., 2014. Dynamic crushing of aluminum foams: Part ii – analysis. International Journal of Solids and Structures 51, 1646 – 1661.

Gaitanaros, S., Kyriakides, S., Kraynik, A.M., 2012. On the crushing response of random open-cell foams. International Journal of Solids and Structures 49, 2733 – 2743. Proceedings of International Union of Theoretical and Applied Mechanics Symposium.

Gerbal, F., Wang, Y., Lyonnet, F., Bacri, J.C., Hocquet, T., Devaud, M., 2015. A refined theory of magnetoelastic buckling matches experiments with ferromagnetic and superparamagnetic rods. Proc. Nat. Acad. Sci. 112, 7135–7140. http://www.pnas.org/content/112/23/7135.full.pdf.

Golubitsky, M., Stewart, I., et al., 2012. Singularities and groups in bifurcation theory. volume 2. Springer Science & Business Media.

Haghpanah, B., Papadopoulos, J., Mousanezhad, D., Nayeb-Hashemi, H., Vaziri, A., 2014. Buckling of regular, chiral and hierarchical honeycombs under a general macroscopic stress state. Proc. R. Soc. a 470, 20130856.

Healey, T.J., Dharmavaram, S., 2017. Symmetry-breaking global bifurcation in a surface continuum phase-field model for lipid bilayer vesicles. SIAM Journal on Mathematical Analysis 49, 1027–1059. https://doi.org/10.1137/15M1043716.

Hibbitt, Karlsson, Sorensen, 1998. ABAQUS/standard: User's Manual. volume 1. Hibbitt, Karlsson & Sorensen.

Huang, R., 2005. Kinetic wrinkling of an elastic film on a viscoelastic substrate. Journal of the Mechanics and Physics of Solids 53, 63–89.

Huang, R., Suo, Z., 2002. Instability of a compressed elastic film on a viscous layer. International Journal of Solids and Structures 39, 1791–1802.

Huang, S., Pessot, G., Cremer, P., Weeber, R., Holm, C., Nowak, J., Odenbach, S., Menzel, A.M., Auernhammer, G.K., 2016. Buckling of paramagnetic chains in soft gels. Soft Matter 12, 228–237.

Hunt, G., 1986. Hidden (a) symmetries of elastic and plastic bifurcation. Applied Mechanics Reviews 39, 1165–1186.

Hunt, G.W., Da Silva, L., Manzocchi, G., 1988. Interactive buckling in sandwich structures. Proc. R. Soc. Lond. A 417, 155–177.

Hunt, G.W., Wadee, M.A., 1998. Localization and mode interaction in sandwich structures, in: Proceedings of the Royal Society of London A: Mathematical, Physical and Engineering Sciences, The Royal Society. pp. 1197–1216.

Hutchinson, J., Koiter, W., 1970. Postbuckling theory. Appl. Mech. Rev 23, 1353–1366.

Jager, E.W., Smela, E., Inganäs, O., 2000. Microfabricating conjugated polymer actuators. Science 290, 1540–1545.

Javid, F., Liu, J., Shim, J., Weaver, J.C., Shanian, A., Bertoldi, K., 2016. Mechanics of instability-induced pattern transformations in elastomeric porous cylinders. Journal of the Mechanics and Physics of Solids 96, 1–17.

Kang, S.H., Shan, S., Košmrlj, A., Noorduin, W.L., Shian, S., Weaver, J.C., Clarke, D.R., Bertoldi, K., 2014. Complex ordered patterns in mechanical instability induced geometrically frustrated triangular cellular structures. Physical review letters 112, 098701.

Karman, T.V., 1939. The buckling of spherical shells by external pressure. Journal of the Aeronautical Sciences 7, 43–50.

Kochmann, D.M., Bertoldi, K., 2017. Exploiting microstructural instabilities in solids and structures: From metamaterials to structural transitions. Applied Mechanics Reviews 69, 050801–050801–24.

Koiter, W.T., Pignataro, M., 1976. An alternative approach to the interaction between local and overall buckling in stiffened panels, in: Buckling of structures. Springer, pp. 133–148.
Kooistra, G.W., Deshpande, V., Wadley, H.N., 2007. Hierarchical corrugated core sandwich panel concepts. Journal of applied mechanics 74, 259–268.
Kothari, M., Cha, M.H., Kim, K.S., 2018. Critical curvature localization in graphene. i. quantum-flexoelectricity effect. Proc. Roy. Soc. A in press.
Lee, A., Jiménez, F.L., Marthelot, J., Hutchinson, J.W., Reis, P.M., 2016. The geometric role of precisely engineered imperfections on the critical buckling load of spherical elastic shells. Journal of Applied Mechanics 83, 111005.
Lee, H., Zhang, J., Jiang, H., Fang, N.X., 2012. Prescribed pattern transformation in swelling gel tubes by elastic instability. Physical Review Letters 108, 214304.
Li, B., Cao, Y.P., Feng, X.Q., Gao, H., 2012. Mechanics of morphological instabilities and surface wrinkling in soft materials: a review. Soft Matter 8, 5728–5745.
Liu, Y., Yu, K., Hu, H., Belouettar, S., Potier-Ferry, M., Damil, N., 2012. A new fourier-related double scale analysis for instability phenomena in sandwich structures. International Journal of Solids and Structures 49, 3077–3088.
Marthelot, J., López Jiménez, F., Lee, A., Hutchinson, J.W., Reis, P.M., 2017. Buckling of a pressurized hemispherical shell subjected to a probing force. Journal of Applied Mechanics 84, 121005–121005–9.
Meza, L.R., Zelhofer, A.J., Clarke, N., Mateos, A.J., Kochmann, D.M., Greer, J.R., 2015. Resilient 3d hierarchical architected metamaterials. Proc. Nat. Acad. Sci. 112, 11502–11507. http://www.pnas.org/content/112/37/11502.full.pdf.
Mousanezhad, D., Babaee, S., Ebrahimi, H., Ghosh, R., Hamouda, A.S., Bertoldi, K., Vaziri, A., 2015. Hierarchical honeycomb auxetic metamaterials. Scientific reports 5, 18306.
Mousanezhad, D., Haghpanah, B., Ghosh, R., Hamouda, A.M., Nayeb-Hashemi, H., Vaziri, A., 2016. Elastic properties of chiral, anti-chiral, and hierarchical honeycombs: a simple energy-based approach. Theoretical and Applied Mechanics Letters 6, 81–96.
Mullin, T., Deschanel, S., Bertoldi, K., Boyce, M.C., 2007. Pattern transformation triggered by deformation. Physical review letters 99, 084301.
Van der Neut, A., 1969. The interaction of local buckling and column failure of thin-walled compression members, in: Applied Mechanics. Springer, pp. 389–399.
Oftadeh, R., Haghpanah, B., Vella, D., Boudaoud, A., Vaziri, A., 2014. Optimal fractal-like hierarchical honeycombs. Physical review letters 113, 104301.
Ohno, N., Okumura, D., Niikawa, T., 2004. Long-wave buckling of elastic square honeycombs subject to in-plane biaxial compression. International journal of mechanical sciences 46, 1697–1713.
Okumura, D., Ohno, N., Noguchi, H., 2004. Elastoplastic microscopic bifurcation and post-bifurcation behavior of periodic cellular solids. Journal of the Mechanics and Physics of Solids 52, 641 – 666.
Papka, S., Kyriakides, S., 1999a. Biaxial crushing of honeycombs:—part 1: Experiments. International Journal of Solids and Structures 36, 4367–4396.
Papka, S., Kyriakides, S., 1999b. In-plane biaxial crushing of honeycombs—: Part ii: Analysis. International Journal of Solids and Structures 36, 4397–4423.
Papka, S.D., Kyriakides, S., 1994. In-plane compressive response and crushing of honeycomb. Journal of the Mechanics and Physics of Solids 42, 1499–1532.
Papka, S.D., Kyriakides, S., 1998. Experiments and full-scale numerical simulations of in-plane crushing of a honeycomb. Acta materialia 46, 2765–2776.
Pipkin, A.C., 1986. Some examples of crinkles, in: ed. J. L. ERIKSEN, D. KINDERLEHRER, R.V.K., LIONS, J.L. (Eds.), Homogenization and Efective Moduli, pp. 182–195.
Psarra, E., Bodelot, L., Danas, K., 2017. Two-field surface pattern control via marginally stable magnetorheological elastomers. Soft Matter 13, 6576–6584.
Russell, B., Deshpande, V., Fleck, N., et al., 2009. The through-thickness compressive strength of a composite sandwich panel with a hierarchical square honeycomb sandwich core. Journal of Applied Mechanics 76, 061004.
Ryvkin, M., Shraga, R., 2018. Fracture toughness of hierarchical self-similar honeycombs. International Journal of Solids and Structures .
Stoop, N., Lagrange, R., Terwagne, D., Reis, P.M., Dunkel, J., 2015. Curvature-induced symmetry breaking determines elastic surface patterns. Nature materials 14, 337–342.
Sun, Y., Chen, Q., Pugno, N., 2014. Elastic and transport properties of the tailorable multifunctional hierarchical honeycombs. Composite Structures 107, 698–710.
Sun, Y., Pugno, N.M., 2013. In plane stiffness of multifunctional hierarchical honeycombs with negative poisson's ratio sub-structures. Composite Structures 106, 681–689.

Taylor, C., Smith, C., Miller, W., Evans, K., 2011. The effects of hierarchy on the in-plane elastic properties of honeycombs. International Journal of Solids and Structures 48, 1330–1339.
Thompson, J., Lewis, G., 1972. On the optimum design of thin-walled compression members. Journal of the Mechanics and Physics of Solids 20, 101–109.
Thompson, J.M.T., Hunt, G.W., 1973. A general theory of elastic stability. J. Wiley London.
Timoshenko, S., Gere, J., 1936. Theory of Elastic Stability. McGraw-Hill Book Company, Incoroporated.
Triantafyllidis, N., Nestorović, M., Schraad, M., 2006. Failure surfaces for finitely strained two-phase periodic solids under general in-plane loading. Journal of Applied Mechanics 73, 505–515.
Trujillo, V., Kim, J., Hayward, R.C., 2008. Creasing instability of surface-attached hydrogels. Soft Matter 4, 564–569.
Tvergaard, V., 1973. Imperfection-sensitivity of a wide integrally stiffened panel under compression. International Journal of Solids and Structures 9, 177–192.
Tvergaard, V., Needleman, A., 1980. On the localization of buckling patterns. Journal of Applied Mechanics 47, 613–619.
Wah, T., 1965. The buckling of gridworks. Journal of the Mechanics and Physics of Solids 13, 1–16.
Wang, L., Lau, J., Thomas, E.L., Boyce, M.C., 2011. Co-continuous composite materials for stiffness, strength, and energy dissipation. Advanced Materials 23, 1524–1529.
Wang, Q., Zhao, X., 2013. Creasing-wrinkling transition in elastomer films under electric fields. Physical Review E 88, 042403.
Wang, Q., Zhao, X., 2016. Beyond wrinkles: Multimodal surface instabilities for multifunctional patterning. MRS Bulletin 41, 115–122.
Xu, F., Potier-Ferry, M., Belouettar, S., Cong, Y., 2014. 3d finite element modeling for instabilities in thin films on soft substrates. International Journal of Solids and Structures 51, 3619–3632.
Yiatros, S., Wadee, M.A., 2010. Interactive buckling in sandwich beam-columns. IMA journal of applied mathematics 76, 146–168.
Zerhouni, O., Tarantino, M., Danas, K., 2019. Numerically-aided 3d printed random isotropic porous materials approaching the hashin-shtrikman bounds. Composites Part B: Engineering 156, 344 – 354.
Zheng, X., Smith, W., Jackson, J., Moran, B., Cui, H., Chen, D., Ye, J., Fang, N., Rodriguez, N., Weisgraber, T., et al., 2016. Multiscale metallic metamaterials. Nature materials 15, 1100.
Zhu, H., Yan, L., Zhang, R., Qiu, X., 2012. Size-dependent and tunable elastic properties of hierarchical honeycombs with regular square and equilateral triangular cells. Acta Materialia 60, 4927–4939.